Journal of
Photonics for Energy

PhotonicsforEnergy.SPIEDigitalLibrary.org

# Poly(vinyl pyrrolidone)-modified metal oxide anode interlayers for stable organic solar cells

Hima A. Kavuri
Shinji Kihara
Duncan J. McGillivray
Geoff Willmott

SPIE.

Hima A. Kavuri, Shinji Kihara, Duncan J. McGillivray, Geoff Willmott, "Poly(vinyl pyrrolidone)-modified metal oxide anode interlayers for stable organic solar cells," *J. Photon. Energy* **10**(4), 042003 (2020), doi: 10.1117/1.JPE.10.042003

# Poly(vinyl pyrrolidone)-modified metal oxide anode interlayers for stable organic solar cells

**Hima A. Kavuri,**[a,*,†] **Shinji Kihara,**[b,c] **Duncan J. McGillivray,**[b,c]
**and Geoff Willmott**[a,b,c]
[a]The University of Auckland, Department of Physics, Auckland, New Zealand
[b]The University of Auckland, School of Chemical Sciences, Auckland, New Zealand
[c]The MacDiarmid Institute for Advanced Materials and Nanotechnology, Wellington, New Zealand

**Abstract.** A new generation of anode interlayers (AILs) has been introduced in recent years for improving the efficiency and stability of organic solar cell (OSC) devices. Electrode interlayer modification is a simple and effective way of enhancing OSC device performance. We used poly(vinyl pyrrolidone) (PVP) as an AIL modifier to alter molybdenum trioxide ($MoO_3$) and vanadium pentoxide ($V_2O_5$) AILs in OSC devices and compared them with pure metal oxide AILs. Using this modification, average power conversion efficiencies were raised from 5.2% ± 0.4% to 6.0% ± 0.3% for OSCs with $MoO_3$-based AILs, and from 6.2% ± 0.1% to 6.8% ± 0.3% for OSCs with $V_2O_5$-based AILs. Moreover, the PVP-metal oxide AILs also improved the overall device quality, producing a nanotextured morphology with good optical properties and favorable chemical composition. Beneficial wetting properties for interfacial adhesion between anode and active layer are observed using contact angle measurements. Overall, devices with PVP-modified metal oxide AILs showed promising results with greater device stability compared to pure metal oxide AIL-based OSC devices. © *2020 Society of Photo-Optical Instrumentation Engineers (SPIE)* [DOI: 10.1117/1.JPE.10.042003]

**Keywords:** interlayer modification; molybdenum trioxide; vanadium pentoxide; PVP-$MoO_3$; PVP-$V_2O_5$; organic solar cell devices.

Paper 19079SS received Aug. 27, 2019; accepted for publication Dec. 19, 2019; published online Feb. 5, 2020.

## 1 Introduction

Organic solar cells (OSCs) have recently reached power conversion efficiencies (PCEs) of up to 16%.[1] A particularly attractive feature of OSCs is the possibility of developing cost-effective large-scale production methods, as devices can be fabricated using solution-processable materials. The typical structure of an OSC (Fig. 1) includes a bulk heterojunction active layer, consisting of a mixture of donor and acceptor materials. Apart from the active layer, interlayers between the active layer and the electrodes play an important role in the extraction of photogenerated charges, affecting the efficiency of the overall OSC device.

In terms of anode interlayers (AILs), poly(3,4-ethylenedioxythiophene)-poly(styrenesulfonate) (PEDOT:PSS) has been almost universally used over the past decade[2,3] on top of an indium tin oxide (ITO) anode. However, the negative effects of PEDOT:PSS on active layer morphology have been well documented and can affect device longevity and overall efficiency.[4–6] These problems have been associated with low charge carrier mobilities and nonradiative recombination losses within the device.[7] These results suggest that even though PEDOT:PSS has served well as a solution-processable AIL, it is unlikely to be the ultimate AIL material in a future OSC technology.

---

[*] Address all correspondence to Hima A. Kavuri, E-mail: hima.kavuri@riken.jp

[†] Present address: RIKEN Center for Emergent Matter Science, 2-1 Hirosawa, Wako-shi, Saitama 351-0198, Japan

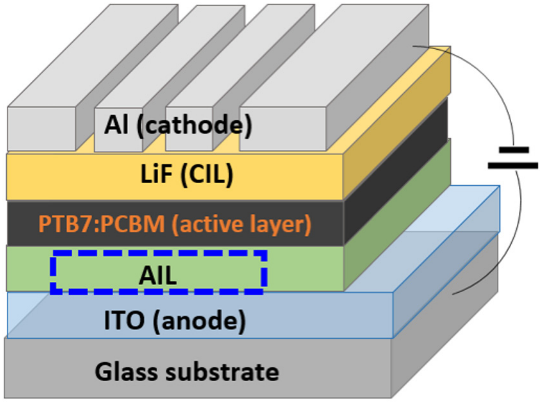

**Fig. 1** Schematic of the OSC device structure studied in this work. The AILs used were $MoO_3$, PVP-$MoO_3$, $V_2O_5$, and PVP-$V_2O_5$.

In recent years, a new generation of AILs has been introduced using materials such as metal oxides,[8–10] conducting polymers,[11] graphene-based AILs,[12] conductive polyelectrolytes,[13] and cross-linkable materials.[14] Semiconductor metal oxide interlayers can have consistent long-term stability in high-efficiency OSCs.[15,16] Among these metal oxides, molybdenum trioxide ($MoO_3$) and vanadium pentoxide ($V_2O_5$) have been widely used to produce AILs processed at low temperatures. The combination of low temperature processing conditions with high PCE motivates the use of metal oxides as AILs in OSC devices.[17]

Electrode interlayer modification using polymers is known to be a simple and effective way to improve OSC device performance.[18,19] For example, metal oxides modified with polymers, such as poly[(9,9-bis(3′-(*N*,*N*-dimethylamino)propyl)-2,7-fluorene)-alt-2,7-(9,9-dioctyl)-fluorene] (PFN) and poly(vinyl pyrrolidone) (PVP), have produced reduced surface defects when the polymer was directly mixed with the metal oxide rather than coated on top as a bilayer.[20,21] PVP is a widely known nonconjugated polymer, which has been used both as a stand-alone cathode interlayer (CIL) in OSCs and as a CIL in combination with metal oxides.[21,22] Most of the interlayer modifications reported so far have involved CILs, especially the use of various polymer composites with zinc oxide (ZnO)[23,24] and titanium oxide ($TiO_x$).[25] In contrast, there are very few reports on metal oxide AIL modifications with polymers in OSC devices, and those reports have mostly used a metal-oxide/polymer bilayer structure.[26] Nanocomposite-based AILs are slowly gaining attention in OSCs due to their structural and optical advantages over pure metal oxide AILs.[27,28] Similar to pure metal oxides,[29,30] the work function of these nanocomposite AILs can also be tuned to align energy levels for a wide range of donor materials.[31] In addition, compared to the complex functionalization methods reportedly required to modify interfacial layers,[32] a simple mixture of alcohol-soluble modifier like PVP and the metal oxide precursors would be more beneficial toward cost-effective large-scale printing of next-generation solar cells.[33] Most of the polymer-based composites for metal oxide AIL modifications have used only PEDOT:PSS.[32,34,35] However, the acidic nature of PEDOT:PSS mixed with water-based metal oxide precursors limits the long-term air stability. Therefore, there is a need for water-free and nonacidic AIL precursors to enhance the air stability along with the efficiency of the OSC devices.

In this work, PVP nanocomposite was used for modification of $MoO_3$ (PVP-$MoO_3$) and $V_2O_5$ (PVP-$V_2O_5$) AILs. The alcohol-soluble PVP mixed metal oxide interlayers are compared with pure metal oxide interlayers. The influence of the nanocomposite on the physical and chemical properties of the AIL was analyzed using various characterization techniques, and the effect on OSC device performance has been measured. In all devices, the active layer that was used is poly (4,8-bis[(2-ethylhexyl)oxy]benzo[1,2-b:4,5-b′]dithiophene-2,6-diyl3-fluoro-2-[(2-ethylhexyl)carbonyl]thieno[3,4-b]thiophenediyl):[6,6]-phenyl-$C_{71}$-butyric acid methyl ester (PTB7:$PC_{71}BM$). PTB7 was chosen due to its expanded absorption spectrum up to the near-infrared wavelength region.[36]

## 2 Experimental Details

### 2.1 *Materials and Solutions*

Prepatterned ITO glass slides with sheet resistance of 15 $\Omega/\text{cm}^2$ were purchased from Kintec Company. Bis(2,4-pentanedionato)molybdenum(VI) dioxide was purchased from Sigma-Aldrich. Vanadium triisopropoxide (VTIPO) was purchased from Alfa Aesar. PTB7 was purchased from 1-Material Inc. $PC_{71}BM$ was purchased from Nano-C. PVP (Mw ~1,300,000 by light-scattering); isopropanol, chlorobenzene, and 1,8-diiodooctane (DIO) were purchased from Sigma-Aldrich. All materials were used without further purification.

A $MoO_3$ precursor solution was freshly prepared by dissolving bis(2,4-pentanedionato) molybdenum(VI) dioxide in isopropanol with a 1:150 w/v ratio. A 0.05 M solution precursor of VTIPO was freshly prepared by dissolving 100 $\mu$L of VTIPO in 8 mL of isopropanol. For PVP-$MoO_3$ interlayers, PVP (1 mg/mL) was initially dissolved in isopropanol solvent and ultrasonicated for 10 min until it formed a clear solution. Bis(2,4-pentanedionato) molybdenum(VI) dioxide or VTIPO was then added to the PVP/isopropanol solution at the same concentration as for the pure $MoO_3$ and $V_2O_5$ solutions. An active layer solution was prepared by dissolving PTB7 (10 mg):$PC_{71}BM$ (13 mg) in chlorobenzene (1 mL) and stirring inside the glovebox overnight at room temperature. DIO (3 vol%) was added to the PTB7:$PC_{71}BM$ solution and stirred at 60°C for 3 h before the deposition process.

### 2.2 *Thin-Film Deposition and Device Fabrication*

Prepatterned ITO glass substrates were sequentially cleaned by ultrasonication with acetone and isopropanol for 10 min each. The surface of the cleaned substrates was treated with a UV–ozone cleaner (Novascan Technologies, Inc.). $MoO_3$, PVP-$MoO_3$, and $V_2O_5$ AIL precursor solutions were deposited on the cleaned ITO substrates by spin coating at 5000 rpm for 30 s in air. PVP-$V_2O_5$ was spin-coated at 6000 rpm for 30 s. The resultant thicknesses were 30 nm for $MoO_3$, PVP-$MoO_3$ and $V_2O_5$ AILs, and 28 nm for PVP-$V_2O_5$. The spin-coated films were annealed at 150°C, and PVP-$MoO_3$ AILs were further treated with a UV–ozone cleaner (Novascan) for 15 min.

After depositing AILs, PTB7:$PC_{71}BM$ blended solutions were spin coated at 1000 rpm for 40 s under nitrogen atmosphere inside a glove box to form a 100-nm thin film without a post-deposition annealing process. The substrates were then transferred to a thermal evaporator to deposit a 1-nm lithium fluoride (LiF) interlayer followed by a 100-nm aluminum (Al) electrode under a base pressure of $3 \times 10^{-7}$ Torr. A mask with a designated active area of 0.1 $\text{cm}^2$ was used during the evaporation process. In total, at least six devices were made for each architecture. A schematic for the OSC devices is shown in Fig. 1.

### 2.3 *Characterization Methods*

The surface morphology of AILs and active layers was analyzed using an MFP-3D Origin atomic force microscopy (AFM) in tapping mode under atmospheric conditions. A UV–visible spectrometer (V650, Jasco) was used to measure the transmittance spectra of films. Work function measurements were carried out in air using AC2 photoelectron spectroscopy (RKI Instruments). The surface energy of the films was estimated using contact angle measurements (KSV Instruments Ltd.). The chemical environment and oxidation states were analyzed using X-ray photoelectron spectroscopy (XPS, The Kratos Axis DLD). The photovoltaic device performance was characterized using a 1-kW Oriel solar simulator with an AM 1.5 G filter as the light source in conjunction with a Keithley 2400 source measurement unit. The best performed devices were kept in a dark room in a nitrogen environment to study their stability for 96 h.

# 3 Results and Discussion

## 3.1 *Physical and Chemical Characterization*

### 3.1.1 *AIL surface morphology*

Tapping mode AFM was performed for morphological analysis of metal oxide and PVP-metal oxide films. The root mean square roughness ($R_{\mathrm{rms}}$) for $MoO_3$ was 2.60 nm, increasing to 8.75 nm for untreated PVP-$MoO_3$ AILs and decreasing to 6.91 nm after UV–ozone treatment [Figs. 2(a)–2(c)]. For $V_2O_5$ and PVP-$V_2O_5$ AILs, $R_{\mathrm{rms}}$ was 1.90 and 6.90 nm, respectively [Figs. 2(d) and 2(e)]. As shown in Fig. 2, there is an obvious structural change from a flat surface for a thin layer of metal oxide on top of ITO to a nanotextured surface with the addition of PVP, consistent with previous reports.[37,38]

The presence of nanoscopic voids appearing in between nanoclusters due to rapid solvent evaporation could be a reason for the higher $R_{\mathrm{rms}}$ of PVP-AILs.[39] PVP has a well-known influence on synthesized metal oxide morphologies.[40] The hydrophobic vinyl groups and hydrophilic carbonyl groups present in PVP can induce shape effects by forming polarized micelles in precursor solutions, leading to the formation of metal oxide nanoclusters.[41] The size and self-assembly of these nanoclusters can be controlled by changing the molecular weight of PVP.[42] Hence, by choosing PVP with the highest available average molecular weight (1,300,000 g/mol), 5–15 nm metal oxide nanoclusters were obtained in Fig. 2.

The agglomeration of clusters can leave parts of the surface uncovered [Fig. 2(b)]. These surfaces would be PVP-rich, which would be detrimental for OSC device performance. Therefore, after postdeposition annealing, we further treated the PVP-$MoO_3$ AILs with UV–ozone for 15 min to remove the upper layer of PVP and form a more uniform top surface, as shown in Fig. 2(c).[21] Unlike untreated PVP-$MoO_3$ AILs, PVP-$V_2O_5$ AIL-based devices worked well without performing any PVP surface removal techniques.

Although higher surface roughness can cause local shorts in thin-film devices, it is not a limiting factor for overall device performance. AILs with $R_{\mathrm{rms}}$ as high as 25 nm have been

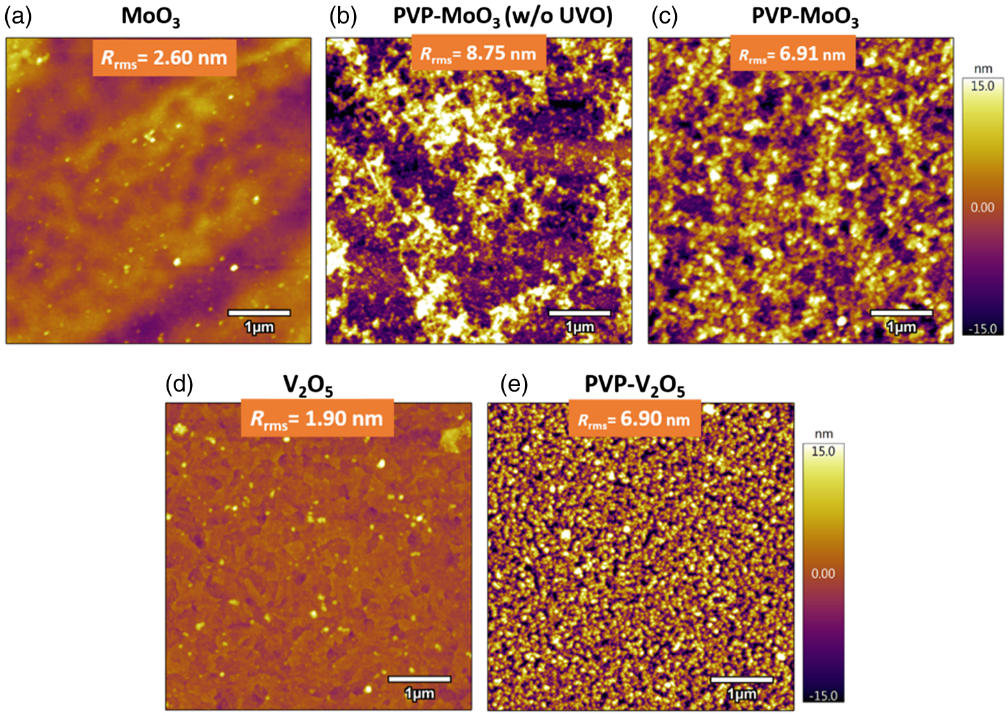

**Fig. 2** Tapping mode AFM images of thin films of (a) $MoO_3$, (b) PVP-$MoO_3$ without UV–ozone treatment (w/o UVO), (c) PVP-$MoO_3$ after UV–ozone treatment, (d) $V_2O_5$, and (e) PVP-$V_2O_5$ thin films.

successfully used as hole injection layers for organic electronic devices.[43] In fact, nanostructured hole-transporting layers can be beneficial for thin-film solar devices by avoiding electronic losses at the electrode/polymer interface, resulting in an increased fill factor (FF)[44,45] and device stability.[46] The surface roughness of active layers deposited on different AILs was also analyzed (see Sec. 5.1). The increment in surface roughness which is required to improve internal reflection in the active layer.[47]

### 3.1.2 *AIL optical properties*

To understand changes in the device performance, the optical transmittance has been analyzed for pure metal oxide AILs with and without the addition of PVP (Fig. 3). A high transmission rate in the visible region could be beneficial for AILs in OSC devices. Figure 3(a) shows that the pure $MoO_3$ layer has slightly less transmittance compared to the PVP-$MoO_3$ composite layers through the visible region. The transmittance of PVP-$MoO_3$ AILs increased after exposure to UV–ozone for 15 min, possibly due to slightly decreased thickness of the layer following removal of the organic layer by UV–ozone treatment. However, the slightly decreased optical transmittance of PVP-$MoO_3$ films below ~400 nm could result in the reduction of short-circuit current density ($J_{SC}$) in OSC devices.[48] There is less difference between the optical transmittance in the case of $V_2O_5$ and PVP-$V_2O_5$ AILs, as shown in Fig. 3(b). In both cases, the highest transmission rate is observed around 500 nm and above, covering most of the solar spectrum. The antireflective effect observed from 330 to 410 nm can be attributed to the formation of smooth surfaces,[49,50] which could decrease the extinction and dispersion of light.

The photoelectron spectroscopy in air technique was used to determine the work function of the AILs presented in Figs. 4(a) and 4(b). These figures plot the square-root of the counting rate as a function of the photon energy in order to find the photoemission threshold energy. The crossing point of the background and the yield line gives the work function of the material.[51,52] The work function for the $MoO_3$ film was determined as 5.7 eV and was decreased to 5.6 eV in the case of PVP-$MoO_3$ AIL [Fig. 4(a)]. The work function was unchanged with and without UV–ozone treatment of AILs. The work function of $V_2O_5$ AILs was 5.5 eV [Fig. 4(b)], only 0.17 eV was lower than the HOMO of the donor PTB7 [Fig. 4(c)]. Hence, holes can more easily travel from the donor's HOMO level to $V_2O_5$ and PVP-$V_2O_5$ AILs and then pass on to the ITO electrode.[53,54] The energy level diagrams shown in Fig. 4(c) were obtained with the values from Figs. 4(a) and 4(b) similar to the previous reports.[52,55,56]

### 3.1.3 *X-ray photoelectron spectroscopy*

XPS core level scans of the Mo 3d region provided an insight into the chemistry of pure and modified $MoO_3$ films. For pure $MoO_3$ [Fig. 5(a)], the intensity is split into two regions that are identified with $3d_{3/2}$ and $3d_{5/2}$ orbitals (the spin-orbit splitting is 3.3 eV) with an area ratio of

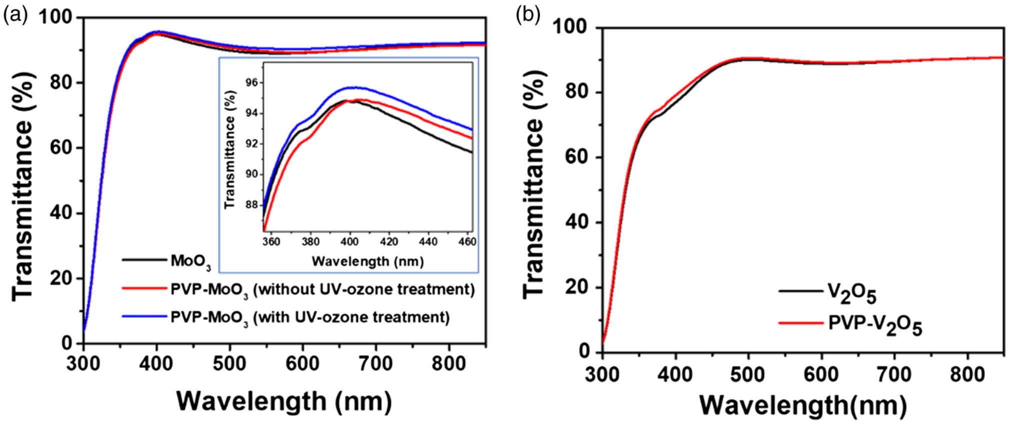

**Fig. 3** Transmittance spectra for (a) $MoO_3$ and PVP-$MoO_3$, with a detailed view of part of the curve inset, and (b) $V_2O_5$ and PVP-$V_2O_5$ AILs.

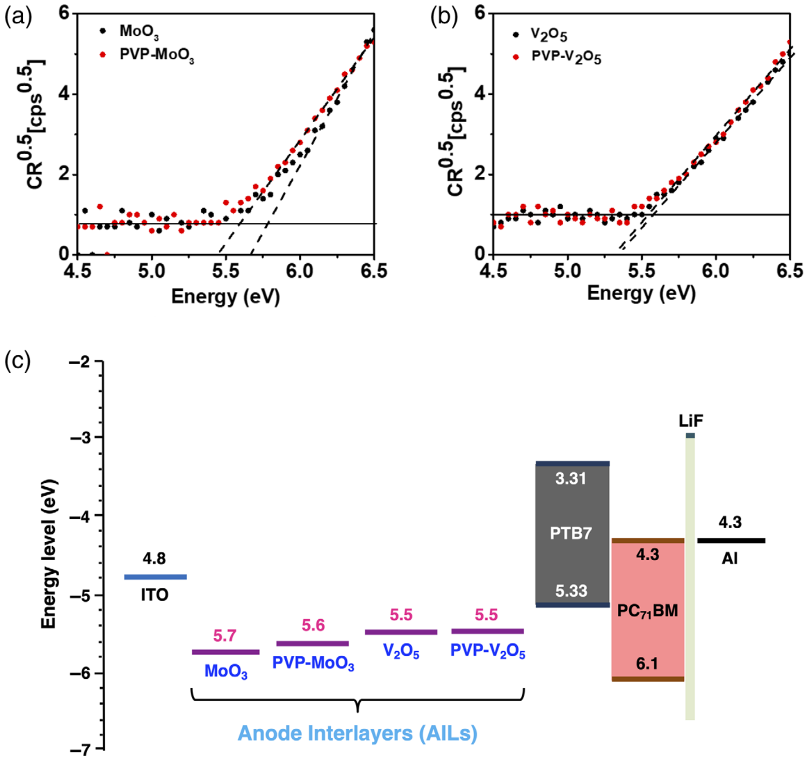

**Fig. 4** Photoelectron spectra for (a) $MoO_3$ and PVP-$MoO_3$, (b) $V_2O_5$ and PVP-$V_2O_5$, and (c) energy level diagrams for AILs with respect to the PTB7 : $PC_{71}BM$ OSC device structure.

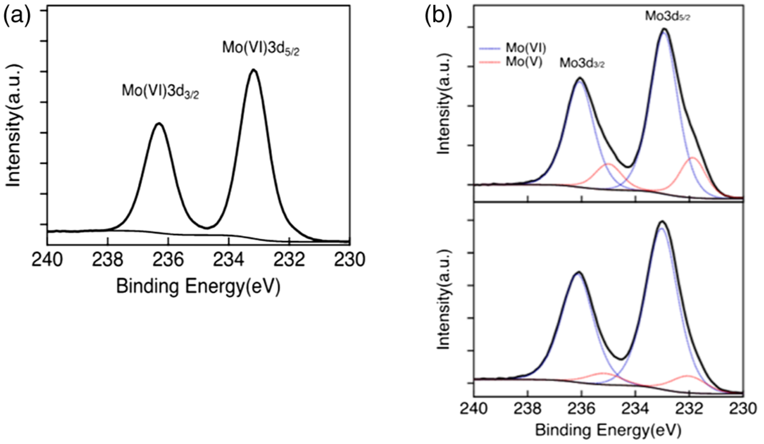

**Fig. 5** XPS Mo 3d core level scans for (a) $MoO_3$ and (b) PVP-$MoO_3$ without UV–ozone (top) and with UV–ozone (bottom) AILs.

1:0.6, respectively. There are no traces of Mo(V) species. These values are consistent with the Mo(VI) state being present in $MoO_3$ AILs.[57]

For PVP-$MoO_3$ with and without UV–ozone treatment [Fig. 5(b)], additional peaks of Mo(V) appear at lower binding energy (by ∼1.0 eV) than the Mo(VI) peaks. Similar spectra were previously reported for different ratios of Mo(V) and Mo(VI) at higher annealing temperatures, from 150°C to 250°C.[58,59] Both of these studies attributed the presence of Mo(V) to distortion of the molybdenum lattice due to gradual dehydration and organic thermalization at elevated temperatures. Since both $MoO_3$ and PVP-$MoO_3$ AILs were annealed at 150°C, the addition of PVP could be the reason behind the observation of Mo(V) states, indicating that some $MoO_3$ lattice distortion had occurred. With the UV–ozone treatment, these peaks attenuated

**Table 1** XPS compositional analysis for $MoO_3$ and PVP-$MoO_3$ AILs. Mo(V):Mo(VI) and Mo:O were calculated using high resolution of Mo 3d and O 1s core level scans.

| AILs | Oxygen (%) | Carbon (%) | Molybdenum (%) | Mo(V):Mo(VI) | Mo:O |
|---|---|---|---|---|---|
| $MoO_3$ | 44.3 | 20.8 | 20.0 | 0.0 | 1:3.0 |
| PVP-$MoO_3$ (without UV–ozone) | 24.4 | 42.8 | 16.7 | 0.2 | 1:2.8 |
| PVP-$MoO_3$ (with UV–ozone) | 43.9 | 25.1 | 18.2 | 0.1 | 1:2.9 |

noticeably, suggesting that the reduced Mo(V) species are forming at the very surface (top ~1 − 3 molecular layers) of the layer and that the UV–ozone treatment effectively suppresses Mo(V) species in PVP-$MoO_3$ AILs. Since these particular $MoO_3$ AIL samples only possess Mo(V) and Mo(VI) species, the minimum Mo:O stoichiometry can be assessed directly from the known Mo(V):Mo(VI) ratios.[58,59] Using ratios obtained from the high-resolution core-level spectra in Fig. 5, the Mo:O stoichiometries of the samples coated on ITO substrates were determined and recorded in Table 1.

A quantitative analysis of the composition of the samples is also listed in Table 1. The relative content of oxygen, carbon, and molybdenum was estimated from O1s, C1s, and Mo 3d core level scans, respectively. The $MoO_3$ AIL has a relatively high oxygen content and almost equal carbon and molybdenum content, with stable Mo:O lattice stoichiometry. PVP-$MoO_3$ without UV–ozone treatment contained less oxygen, with relatively high carbon and low molybdenum content. After UV treatment, the PVP-$MoO_3$ sample has relatively low carbon and molybdenum content. As pointed out before, the atomic ratio of Mo(V):Mo(VI) has decreased from 0.2 to 0.1 after UV–ozone treatment. The resulting calculated stoichiometries are PVP-$MoO_{2.8}$ before UV–ozone treatment and PVP-$MoO_{2.9}$ after UV–ozone treatment. Previous reports have obtained similar values for solution-processed $MoO_3$ AILs and have shown that low annealing temperatures are more suitable for achieving stable Mo:O stoichiometries with less oxygen deficiencies.[60]

From the XPS fits in Fig. 6, we can deduce the presence of two vanadium oxidation states in $V_2O_5$-based AILs by deconvoluting two peaks from the vanadium $V2p_{3/2}$ peak. Namely, V(IV)

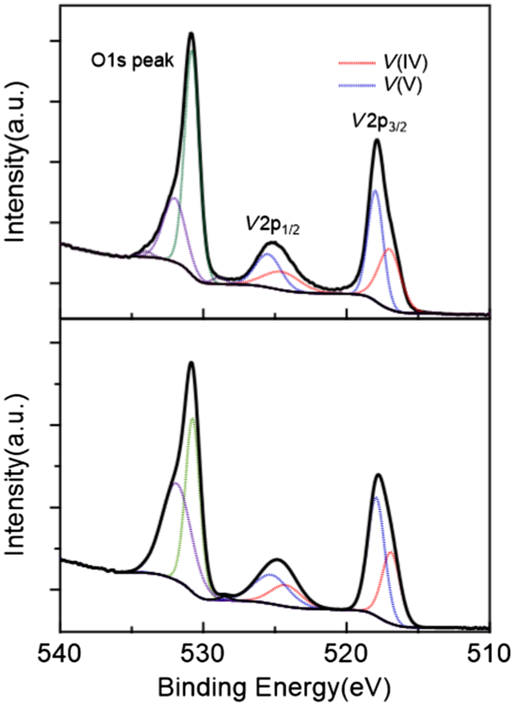

**Fig. 6** O1s and V2p core level scans for $V_2O_5$ (top) and PVP-$V_2O_5$ (bottom) AILs.

**Table 2** XPS data obtained for different $V_2O_5$-based AILs from high resolution scans.

| AIL | V(V) position (eV) | V(IV) position (eV) | V(V):V(IV) | O1s position in $V_2O_5$ (eV) | O1s position in undecomposed precursor (eV) | $V_{OX}$ |
|---|---|---|---|---|---|---|
| $V_2O_5$ | 518.0 | 517.0 | 1.71:1 | 530.8 | 531.9 | 5.1 |
| PVP-$V_2O_5$ | 517.5 | 516.5 | 1.32:1 | 530.7 | 531.9 | 4.8 |

generates a peak between 517 and 516 eV, and V(V) produces a peak at around 518 eV.[61] V(IV) occurs as a result of the partial reduction of V(V) after exposure to air for 10 min. Interestingly, the fraction of V(IV) species slightly increased for the PVP-$V_2O_5$ films, which indicates that more oxygen vacancies are generated during hydrolysis. This could lead to enhanced electrical conductivity of films.[62]

The O1s peak is also fitted using two contributing peaks, which are the peaks for O atoms in $V_2O_5$ between 530.7 and 530.8 eV,[61,63,64] and the undecomposed precursor peak between 531.3 and 531.9 eV.[65] The effective oxidation state of vanadium ($V_{OX}$) can be calculated using the splitting between the O1s and V2p$_{3/2}$ transition centroids, so that $V_{OX} = 13.82 - 0.68 [\mathrm{O(1s)} - \mathrm{V(2p_{3/2})}]$.[66] The values of $V_{OX}$ listed in Table 2 are in agreement with $V_2O_5$ oxidation states from previous reports.[67]

### 3.1.4 *Wettability of AILs*

Wettability measurements can provide information on interfacial interactions between the anode and the active layer in an OSC device.[68] From Figs. 7(a) and 7(b), the surfaces of the $MoO_3$-based AILs clearly become more hydrophilic after the addition of PVP. There was a corresponding small increase in the contact angle for nonpolar chlorobenzene [Figs. 7(c) and 7(d)], which could produce diminished $J_{SC}$ in an OSC device.[69] In contrast, Figs. 8(a) and 8(b) show that water contact angles increased for $V_2O_5$ AILs when PVP was added. This suggests that $V_2O_5$ is less hydrophobic than PVP-$V_2O_5$, which is consistent with the slightly lower contact angles for chlorobenzene on pure $V_2O_5$ [Figs. 8(c) and 8(d)].

In previous work on hole transporting layers, Manders et al. and Cho et al. have demonstrated that hydrophobic AILs result in favorable OSC device characteristics compared to hydrophilic surfaces.[69,70] Moreover, hydrophilic surfaces coated beneath polymer:$PC_{71}BM$ active layers have resulted in adverse aggregation of $PC_{71}BM$, which, in turn, resulted in lower PCE.[71] The decrease in chlorobenzene contact angle on PVP-$V_2O_5$ AILs could therefore lead to strong interfacial cohesion between the anode and the active layer, low series resistance in the OSC device, and consequently enhanced photovoltaic parameters.

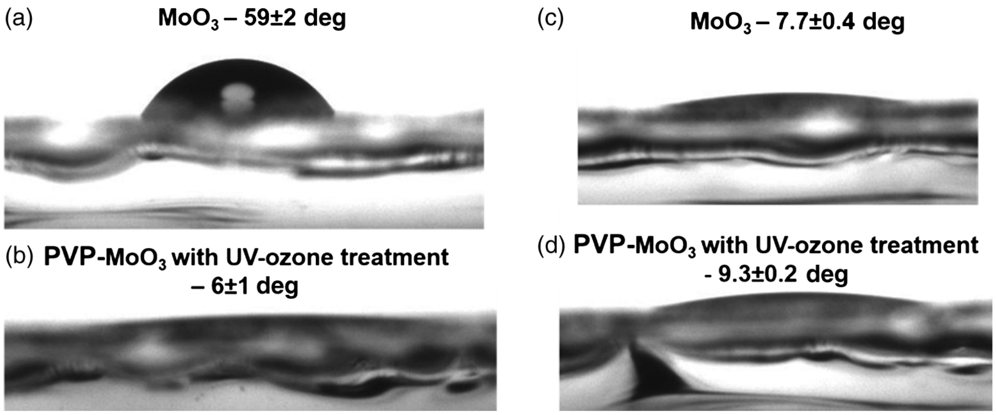

**Fig. 7** (a) and (b) Side-on photographs of droplets of water; (c) and (d) chlorobenzene on the labeled $MoO_3$-based AIL surfaces. Measurements of contact angle are also labeled.

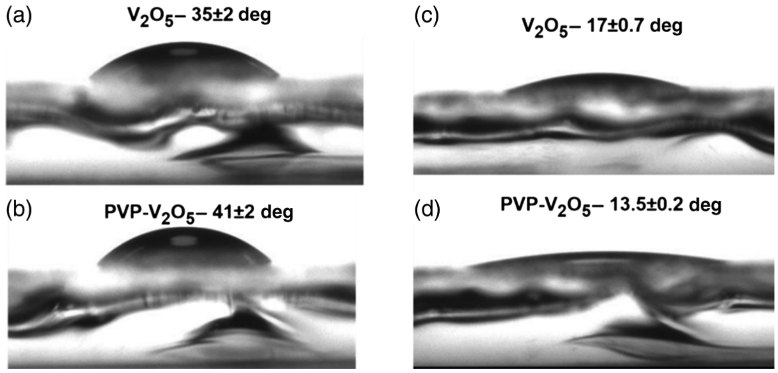

**Fig. 8** (a) and (b) Side-on photographs of droplets of water; (c) and (d) chlorobenzene on the labeled $V_2O_5$-based AIL surfaces. Measurements of contact angle are also labeled.

## 3.2 *Photovoltaic Performance and Stability*

The photovoltaic performance of OSC devices with PVP composite metal oxide AILs was tested and compared with OSCs, which have pure metal oxide AILs. The four OSC device structures for these experiments are shown, as indicated in Fig. 1. Based on topographical measurements (above), oxide encapsulation of PVP[22] seems to be high for PVP-$MoO_3$ AILs, and OSC devices showed diminished performance (PCE = ∼0%) without performing the UV–ozone treatment described previously to remove PVP. Therefore, device analysis for the high efficiency of low band-gap polymer donor PTB7 was carried out only for the best performed AILs; that is, PVP-$MoO_3$ with UV–ozone treatment was studied.

Photovoltaic performance and stability data are presented in Fig. 9 and Table 3. The best efficiency for a single device was obtained with a PVP-$V_2O_5$ AIL, with $V_{OC} = 0.72$ V,

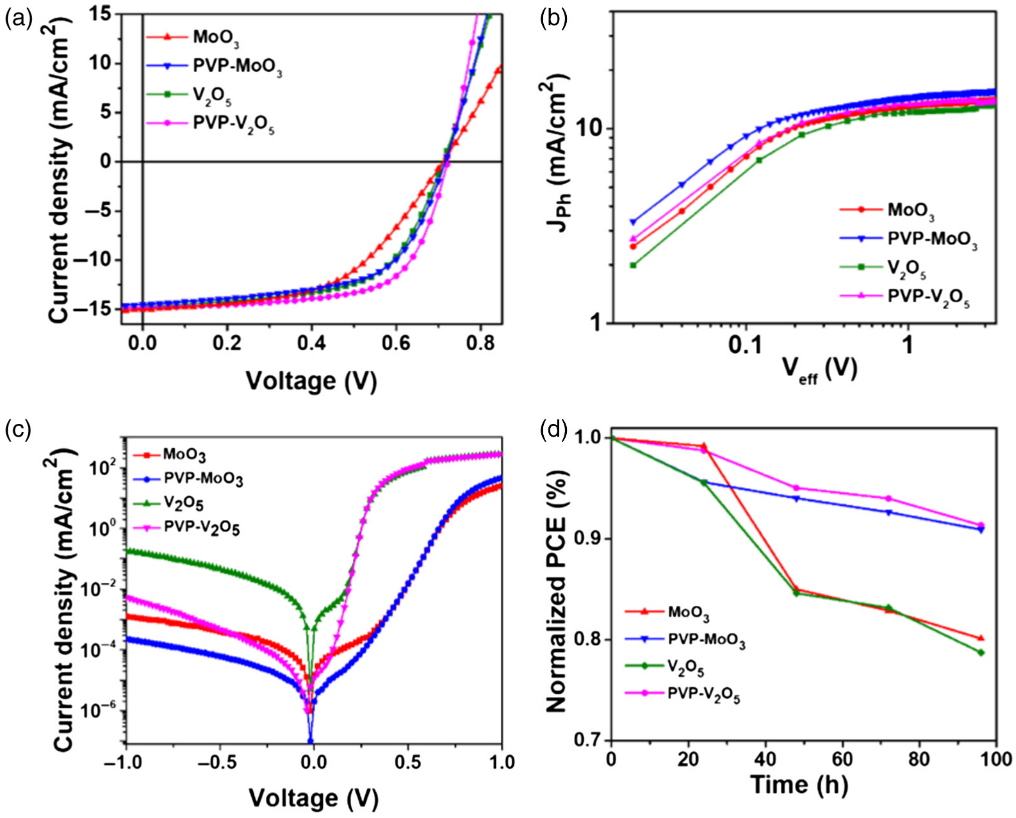

**Fig. 9** Performance and stability data for the best OSCs with various interlayers. (a) *J–V* curves, (b) $J_{Ph}$–$V_{eff}$ characteristics, (c) dark *J–V* curves, and (d) normalized PCE as a function of time.

**Table 3** Photovoltaic parameters for PTB7:$PC_{71}$BM OSCs with various AILs. Mean and standard deviation values are presented for six devices of each type. Shunt ($R_{SH}$) and series ($R_S$) resistances were calculated from the $J$–$V$ curves [Fig. 9(a)].

| AIL | $V_{OC}$ (V) | $J_{SC}$ (mA/cm$^2$) | FF | $PCE_{ave}$ (%) | $PCE_{best}$ (%) | $R_{SH}$ (Ω.cm$^2$) | $R_S$ (Ω.cm$^2$) |
|---|---|---|---|---|---|---|---|
| $MoO_3$ | $0.70 \pm 0.02$ | $15.0 \pm 0.7$ | $0.53 \pm 0.03$ | $5.2 \pm 0.4$ | 5.60 | 714.50 | 15.3 |
| PVP-$MoO_3$ (with UVO) | $0.72 \pm 0.01$ | $14.5 \pm 0.2$ | $0.60 \pm 0.01$ | $6.0 \pm 0.3$ | 6.30 | 1790.50 | 8.1 |
| $V_2O_5$ | $0.72 \pm 0.01$ | $14.7 \pm 0.3$ | $0.60 \pm 0.02$ | $6.2 \pm 0.1$ | 6.32 | 1209 | 8.4 |
| PVP-$V_2O_5$ | $0.72 \pm 0.01$ | $14.8 \pm 0.1$ | $0.66 \pm 0.01$ | $6.8 \pm 0.3$ | 7.10 | 1396 | 6.1 |

$J_{SC} = 14.82\ \mathrm{mA/cm^2}$, FF = 66%, and a PCE of 7.10%. The slight dip in the current-density in devices with AILs of PVP-$MoO_3$ following UV–ozone treatment, in comparison to devices with $MoO_3$ interlayers, can be explained by the increasing surface roughness (from 2.60 to 6.91 nm), which can lead to the formation of local shorts in the interlayer.[18,72] On the other hand, the increment in FF from 0.53 (for $MoO_3$) to 0.60 (for PVP-$MoO_3$) shows improvement in the OSC device quality with the addition of PVP. Also, $V_{OC}$ is enhanced for PVP-$MoO_3$ AILs compared with $MoO_3$ AILs, from 0.70 to 0.72 V. These improvements in FF and $V_{OC}$ can be attributed to efficient hole transportation because of the reduced work function of the PVP-$MoO_3$ AILs. The hydrophilic nature of the PVP-$MoO_3$ AIL surface is also consistent with the decrease in $J_{SC}$ relative to pure $MoO_3$, but this did not offset the increased FF measurement.

Similar enhancement in FF was seen in PVP-$V_2O_5$ compared to pure $V_2O_5$-based devices. The enhancement in $V_{OC}$ to 0.72 V for $V_2O_5$ and PVP-$V_2O_5$ compared to $MoO_3$-based devices can be explained by more efficient charge transfer because of the reduced work function of $V_2O_5$ layers. Wettability of the AILs seems to have no large effect on the overall device performance although the hydrophobic $MoO_3$ AIL, which could have stronger adhesion with the active layer showed slightly higher $J_{SC}$.

The PTB7:$PC_{71}$BM devices were also measured in reverse bias conditions to better understand their performance with respect to the addition of PVP nanocomposite. As shown in Fig. 9(b), the photocurrent density ($J_{Ph}$) increases with effective voltage ($V_{eff}$)[73] and reaches saturation at ~2 V, suggesting that most of the electron–hole pairs are dissociated into free carriers at this potential. Since the photocurrent generation mechanism is dependent on the quality of charge carrier injection and extraction rates, at any given point in the device only a certain number of electron–hole (e–h) pairs can dissociate and transfer to appropriate electrodes. For the maximum power output condition ($V_{eff} = 0.2$ V), $J_{Ph}/J_{Sat}$ is 0.85, 0.90, 0.87, and 0.96 for the best-performed $MoO_3$, PVP-$MoO_3$, $V_2O_5$, and PVP-$V_2O_5$ AIL OSC devices, respectively. The high values of $V_{OC}$ and FF observed for PVP-$V_2O_5$ AIL-based OSC devices can be partly attributed to efficient charge extraction at the AIL/active layer interface, with suppressed nongeminate recombination leading to an improved collection of charge carriers at the respective electrodes.[74]

In Fig. 9(c), the lowest leakage current of $1.87 \times 10^{-4}\ \mathrm{mA/cm^2}$ was obtained for a PVP-$MoO_3$ device. This is one order of magnitude less than the leakage current for the best-performed pure $MoO_3$ and PVP-$V_2O_5$ AIL-based devices. This result is consistent with the high shunt resistance ($R_{SH}$) of 1790.5 Ω.cm$^2$ and the moderately low series resistance ($R_S$) of 8.10 Ω.cm$^2$ recorded in Table 3 for PVP-$MoO_3$ AIL devices.

Stability was also studied for PTB7:$PC_{71}$BM solar cell devices with the various AILs [Fig. 9(d)]. After 96 h, $MoO_3$ and PVP-$MoO_3$ AIL devices had decreases in $J_{SC}$ of 20% and 17%, and in FF of 5.6% and 4.9%, respectively. This led to efficiency retention of 81% and 91% for $MoO_3$ and PVP-$MoO_3$ OSC devices, respectively. The $V_2O_5$ AIL-based device showed a 9.5% reduction in $J_{SC}$ and a 4.5% reduction in FF, retaining 79% of its initial PCE. For the PVP-$V_2O_5$ device, $J_{SC}$ decreased 10.5% and only 1.8% in FF, with 91% retention of PCE. Overall, the PVP nanocomposite metal oxide AIL devices had better efficiency retention than pure metal oxide AIL devices. This enhanced stability is likely to be due to the nonacidic nature of the PVP-modified metal AILs.

## 4 Conclusion

In summary, the results have demonstrated that solution-processible PVP nanocomposite metal oxide AILs showed distinctive nanotextured morphology with higher transmittance compared to pure metal oxide AILs. Both PVP mixed metal oxides also showed favorable chemical composition, thereby producing improved photovoltaic performance compared to pure metal oxide AILs. They exhibited greater stability (higher efficiency retention) and better shunt resistance ($R_{SH}$) with lower leakage currents. The results suggest that charge extraction within OSC devices was more efficient for the PVP nanocomposites. This photovoltaic performance in conjunction with the optical, chemical, and interfacial properties suggest that the PVP nanocomposite metal oxide AILs could give not only unperturbed diode characteristics but could also improve the photovoltaic parameters of OSC devices. Indeed, the clear increase in FF for PVP-based AILs indicates an enhancement in the overall device quality. Thus, PVP-metal oxide mixtures provide promising AILs. One of the reasons to extend this study to PVP-$V_2O_5$ was to avoid UV–ozone treatment, which was necessary for removal of a surface organic layer on PVP-$MoO_3$ AILs, and therefore to achieve enhanced photovoltaic performance without this additional fabrication procedure. These results demonstrate the potential for AILs processed at moderate annealing temperatures with simple fabrication procedures to improve the overall quality and stability of OSC devices.

## 5 Appendix

### 5.1 *Surface Morphology of Active Layers*

The differences in surface roughness for the active layer were comparatively small for devices with $MoO_3$ AILs [Figs. 10(a)–10(c)]. $R_{rms}$ for PTB7∶$PC_{71}$BM coated on pure $MoO_3$ was 2.40 nm. This increased to 2.85 nm for coating on untreated PVP-$MoO_3$ and increased slightly further to 2.90 nm for coating on UV–ozone treated PVP-$MoO_3$. An increase in the surface roughness of active layers was consistently observed with the addition of PVP to the $V_2O_5$

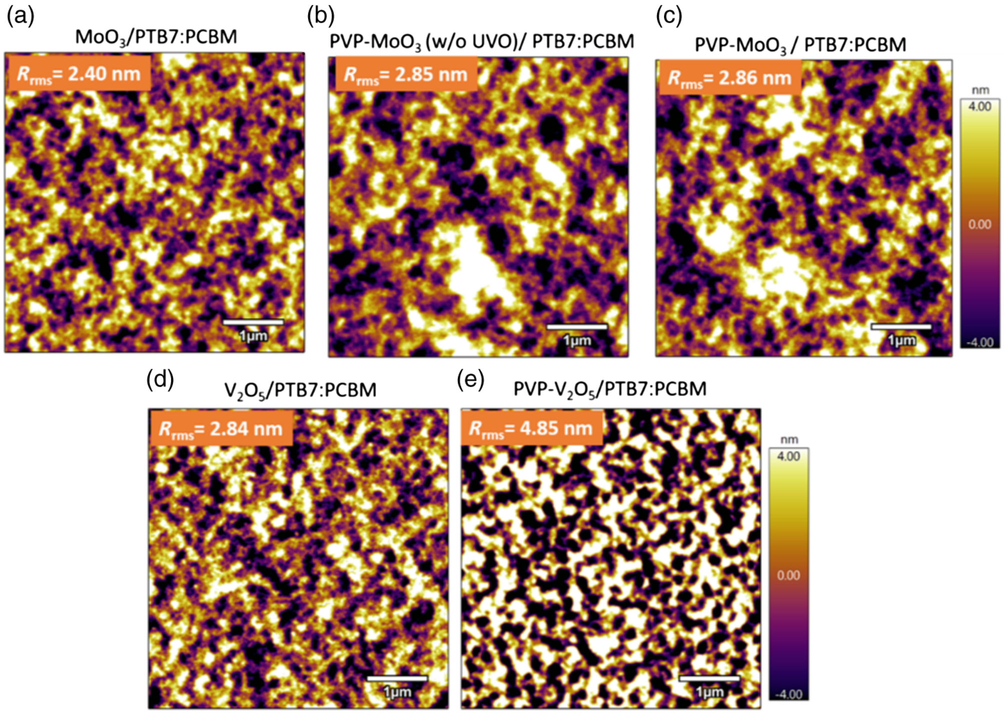

**Fig. 10** AFM images of PTB7∶$PC_{71}$BM active layers coated on (a) $MoO_3$, (b) PVP-$MoO_3$ without UV–ozone treatment (w/o UVO), (c) PVP-$MoO_3$ after UV–ozone treatment, (d) $V_2O_5$, and (e) PVP-$V_2O_5$.

AILs. For active layers deposited on $V_2O_5$ AIL, the $R_{\mathrm{rms}}$ value was 2.84 nm and this increased to 4.85 nm for PVP-$V_2O_5$ layers [Figs. 10(d) and 10(e)]. Rough surfaces of PTB7 : $PC_{71}BM$ layers can improve the internal reflection in the active layer, which can lead to increased device efficiency.[47]

## Acknowledgments

This work was supported by New Zealand's Ministry of Business, Innovation and Employment (Contract UOAX0911), the Faculty of Science at the University of Auckland, and a Universitas 21 Graduate Research Project grant. The authors thank Dr. Yiran An for providing technical support with AFM and Dr. Krishnachary Salikolimi for providing photoelectron spectroscopy measurements. The authors wish to thank Dr. Jegadesan Subbiah and Dr. David Jones at the University of Melbourne for providing facilities and expert advice for some parts of this research.

## References

1. B. Fan et al., "Achieving over 16% efficiency for single-junction organic solar cells," *Sci. China Chem.* **62**(6), 746–752 (2019).
2. F. Zhang et al., "Polymer photovoltaic cells with conducting polymer anodes," *Adv. Mater.* **14**(9), 662–665 (2002).
3. S.-I. Na et al., "Efficient and flexible ITO-free organic solar cells using highly conductive polymer anodes," *Adv. Mater.* **20**(21), 4061–4067 (2008).
4. M. F. Al-Mudhaffer et al., "The origin of performance limitations in miniemulsion nanoparticulate organic photovoltaic devices," *Sol. Energy Mater. Sol. Cells* **175**, 77–88 (2018).
5. F. Liu et al., "Understanding the morphology of PTB7:PCBM blends in organic photovoltaics," *Adv. Energy Mater.* **4**(5), 1301377 (2014).
6. M. Jørgensen, K. Norrman, and F. C. Krebs, "Stability/degradation of polymer solar cells," *Sol. Energy Mater. Sol. Cells* **92**(7), 686–714 (2008).
7. A. Uddin and X. Yang, "Surface plasmonic effects on organic solar cells," *J. Nanosci. Nanotechnol.* **14**(2), 1099–1119 (2014).
8. Y. Sun et al., "Solution-processed small-molecule solar cells with 6.7% efficiency," *Nat. Mater.* **11**(1), 44–48 (2012).
9. M. Y. Ameen et al., "Solution processed transition metal oxide anode buffer layers for efficiency and stability enhancement of polymer solar cells," *Opt. Mater.* **75**, 491–500 (2018).
10. W. Qiu et al., "Ultrathin ammonium heptamolybdate films as efficient room-temperature hole transport layers for organic solar cells," *ACS Appl. Mater. Interfaces* **6**(18), 16335–16343 (2014).
11. J. E. Yoo et al., "Directly patternable, highly conducting polymers for broad applications in organic electronics," *Proc. Natl. Acad. Sci. U. S. A.* **107**(13), 5712–5717 (2010).
12. Y. J. Jeon et al., "Moderately reduced graphene oxide as hole transport layer in polymer solar cells via thermal assisted spray process," *Appl. Surf. Sci.* **296**, 140–146 (2014).
13. H. Zhou et al., "Conductive conjugated polyelectrolyte as hole-transporting layer for organic bulk heterojunction solar cells," *Adv. Mater.* **26**(5), 780–785 (2014).
14. A. W. Hains et al., "Anode interfacial tuning via electron-blocking/hole-transport layers and indium tin oxide surface treatment in bulk-heterojunction organic photovoltaic cells," *Adv. Funct. Mater.* **20**(4), 595–606 (2010).
15. Y. Sun et al., "Efficient, air-stable bulk heterojunction polymer solar cells using $MoO_x$ as the anode interfacial layer," *Adv. Mater.* **23**(19), 2226–2230 (2011).
16. Z. Yin et al., "Interface control of semiconducting metal oxide layers for efficient and stable inverted polymer solar cells with open-circuit voltages over 1.0 volt," *ACS Appl. Mater. Interfaces* **5**(18), 9015–9025 (2013).
17. K. Zilberberg et al., "Low-temperature, solution-processed $MoO_x$ for efficient and stable organic solar cells," *ACS Appl. Mater. Interfaces* **4**(3), 1164–1168 (2012).
18. H. Pan et al., "$MoO_3 - Au$ composite interfacial layer for high efficiency and air-stable organic solar cells," *Org. Electron.* **14**(3), 797–803 (2013).

19. X. Jia et al., "A low-cost and low-temperature processable zinc oxide-polyethylenimine (ZnO:PEI) nano-composite as cathode buffer layer for organic and perovskite solar cells," *Org. Electron. Phys. Mater. Appl.* **38**, 150–157 (2016).
20. N. Wu et al., "Zinc oxide: conjugated polymer nanocomposite as cathode buffer layer for solution processed inverted organic solar cells," *Sol. Energy Mater. Sol. Cells* **141**, 248–259 (2015).
21. C. E. Small et al., "High-efficiency inverted dithienogermole-thienopyrrolodione-based polymer solar cells," *Nat. Photonics* **6**(2), 115–120 (2012).
22. H. Sun et al., "Investigating the multiple roles of polyvinylpyrrolidone for a general methodology of oxide encapsulation," *J. Am. Chem. Soc.* **135**(24), 9099–9110 (2013).
23. S. Shao et al., "Enhanced performance of inverted polymer solar cells by using poly(ethylene oxide)-modified ZnO as an electron transport layer," *ACS Appl. Mater. Interfaces* **5**(2), 380–385 (2013).
24. J. Liu et al., "Printable highly conductive conjugated polymer sensitized ZnO NCs as cathode interfacial layer for efficient polymer solar cells," *ACS Appl. Mater. Interfaces* **6**(11), 8237–8245 (2014).
25. Z. Yin et al., "Solution-derived poly(ethylene glycol)-$TiO_x$ nanocomposite film as a universal cathode buffer layer for enhancing efficiency and stability of polymer solar cells," *Nano Res.* **8**(2), 456–468 (2015).
26. Y. Guo et al., "Organic solar cells based on a $Cu_2O$/FBT-$TH_4$ anode buffer layer with enhanced power conversion efficiency and ambient stability," *J. Mater. Chem. C* **5**(32), 8033–8040 (2017).
27. J. Cheng et al., "Pre- and post-treatments free nanocomposite based hole transport layer for high performance organic solar cells with considerably enhanced reproducibility," *Nano Energy* **34**, 76–85 (2017).
28. Z. Huang et al., "All-room-temperature solution-processed new nanocomposites based hole transport layer from synthesis to film formation for high-performance organic solar cells towards ultimate energy-efficient fabrication," *Nano Energy* **47**, 26–34 (2018).
29. A. L. F. Cauduro et al., "Crystalline molybdenum oxide thin-films for application as interfacial layers in optoelectronic devices," *ACS Appl. Mater. Interfaces* **9**(8), 7717–7724 (2017).
30. X. Li et al., "$MoO_x$ and $V_2O_x$ as hole and electron transport layers through functionalized intercalation in normal and inverted organic optoelectronic devices," *Light Sci. Appl.* **4**, e273 (2015).
31. L. Dou et al., "25th anniversary article: a decade of organic/polymeric photovoltaic research," *Adv. Mater.* **25**(46), 6642–6671 (2013).
32. D. Konios et al., "Highly efficient organic photovoltaic devices utilizing work-function tuned graphene oxide derivatives as the anode and cathode charge extraction layers," *J. Mater. Chem. A* **4**, 1612–1623 (2016).
33. A. Rajagopal, K. Yao, and A. K. Y. Jen, "Toward perovskite solar cell commercialization: a perspective and research roadmap based on interfacial engineering," *Adv. Mater.* **30**, 1800455 (2018).
34. L. Chen et al., "Efficient bulk heterojunction polymer solar cells using PEDOT/PSS doped with solution-processed $MoO_3$ as anode buffer layer," *Sol. Energy Mater. Sol. Cells* **102**, 66–70 (2012).
35. S. Shao et al., "In situ formation of $MoO_3$ in PEDOT:PSS matrix: a facile way to produce a smooth and less hygroscopic hole transport layer for highly stable polymer bulk heterojunction solar cells," *Adv. Energy Mater.* **3**(3), 349–355 (2013).
36. A. Iwan et al., "Electrochemical and photocurrent characterization of polymer solar cells with improved performance after GO addition to the PEDOT:PSS hole transporting layer," *Sol. Energy* **146**, 230–242 (2017).
37. C. V. Subba Reddy et al., "Characterization of $MoO_3$ nanorods for lithium battery using PVP as a surfactant," *J. Solid State Electrochem.* **13**(12), 1945–1949 (2008).
38. P. Gouma, K. Kalyanasundaram, and A. Bishop, "Electrospun single-crystal $MoO_3$ nanowires for biochemistry sensing probes," *J. Mater. Res.* **21**(11), 2904–2910 (2006).
39. X. Orignac et al., "Influence of solvent concentration on the microstructure of $SiO_2$-$TiO_2$ sol-gel films," *J. Sol-Gel Sci. Technol.* **8**(1–3), 243–248 (1997).

40. Z. Gou et al., “Morphology-controllable synthesis and gas-sensing properties of $\alpha$-$MoO_3$,” *J. Mater. Sci. Mater. Electron.* **24**(3), 1018–1023 (2013).
41. D. W. Su, S. X. Dou, and G. X. Wang, “Hierarchical orthorhombic $V_2O_5$ hollow nanospheres as high performance cathode materials for sodium-ion batteries,” *J. Mater. Chem. A* **2**(29), 11185–11194 (2014).
42. Y.-T. Wang, W.-T. Whang, and C.-H. Chen, “Hollow $V_2O_5$ nanoassemblies for high-performance room-temperature hydrogen sensors,” *ACS Appl. Mater. Interfaces* **7**(16), 8480–8487 (2015).
43. J. Meyer et al., “$MoO_3$ films spin-coated from a nanoparticle suspension for efficient hole-injection in organic electronics,” *Adv. Mater.* **23**(1), 70–73 (2011).
44. J. He et al., “Realization of 13.6% efficiency on 20 $\mu$m thick Si/organic hybrid heterojunction solar cells via advanced nanotexturing and surface recombination suppression,” *ACS Nano* **9**(6), 6522–6531 (2015).
45. P. Yu et al., “13% Efficiency hybrid organic/silicon-nanowire heterojunction solar cell via interface engineering,” *ACS Nano* **7**(12), 10780–10787 (2013).
46. N. K. Elumalai et al., “Enhancing the stability of polymer solar cells by improving the conductivity of the nanostructured $MoO_3$ hole-transport layer,” *Phys. Chem. Chem. Phys.* **15**, 6831–6841 (2013).
47. M. V. Srinivasan et al., “Performance evaluation of PTB7:$PC_{71}BM$ based organic solar cells fabricated by spray coating method using chlorine free solvent,” *RSC Adv.* **5**(69), 56262–56269 (2015).
48. S. R. Hammond et al., “Low-temperature, solution-processed molybdenum oxide hole-collection layer for organic photovoltaics,” *J. Mater. Chem.* **22**(7), 3249 (2012).
49. X. Bao et al., “Simple $O_2$ plasma-processed $V_2O_5$ as an anode buffer layer for high-performance polymer solar cells,” *ACS Appl. Mater. Interfaces* **7**(14), 7613–7618, (2015).
50. S.-I. Na et al., “Evolution of nanomorphology and anisotropic conductivity in solvent-modified PEDOT:PSS films for polymeric anodes of polymer solar cells,” *J. Mater. Chem.* **19**(47), 9045–9053 (2009).
51. M. M. Y. A. Alsaif et al., “Exfoliation solvent dependent plasmon resonances in two-dimensional sub-stoichiometric molybdenum oxide nanoflakes,” *ACS Appl. Mater. Interfaces* **8**(5) 3482–3493 (2016).
52. C. Chen, Y. Chen, and S. Chuang, “High-performance and highly durable inverted organic photovoltaics embedding solution-processable vanadium oxides as an interfacial hole-transporting layer,” *Adv. Mater.* **23**(33), 3859–3863 (2011).
53. M. T. Greiner et al., “Universal energy-level alignment of molecules on metal oxides,” *Nat. Mater.* **11**(1), 76–81 (2012).
54. Z. Tan et al., “High-performance inverted polymer solar cells with solution-processed titanium chelate as electron-collecting layer on ITO electrode,” *Adv. Mater.* **24**(11), 1476–1481 (2012).
55. F. Liu et al., “Efficient polymer photovoltaic cells using solution-processed $MoO_3$ as anode buffer layer,” *Sol. Energy Mater. Sol. Cells* **94**(5), 842–845 (2010).
56. F. Cheng et al., “Enhancing the performance and stability of organic solar cells using solution processed $MoO_3$ as hole transport layer,” *RSC Adv.* **7**, 37952–37958 (2017).
57. NIST, “NIST X-ray photoelectron spectroscopy database, NIST standard reference database 20, version 4.1,” 2017, http://srdata.nist.gov/xps/Default.aspx.
58. J. J. Jasieniak et al., “A solution-processed $MoO_x$ anode interlayer for use within organic photovoltaic devices,” *Adv. Funct. Mater.* **22**(12), 2594–2605 (2012).
59. J. Xiong et al., “High alcohol-soluble $MoO_x$ gel for interfacial layer in organic solar cells,” *Curr. Appl. Phys.* **17**(8), 1021–1028 (2017).
60. B. Li et al., “Room-temperature, solution-processed $MoO_x$ thin film as a hole extraction layer to substitute PEDOT/PSS in polymer solar cells,” *ACS Photonics* **1**(2), 87–90 (2014).
61. Y. Suchorski et al., “Evolution of oxidation states in vanadium-based catalysts under conventional XPS conditions,” *Appl. Surf. Sci.* **249**(1), 231–237 (2005).
62. H. Cong et al., “A facile approach to prepare a vanadium oxide hydrate layer as a hole transport layer for high-performance polymer solar cell,” *ACS Appl. Mater. Interfaces* **9**(21) 18087–18094 (2017).

63. D. Briggs, “Auger and X-ray photoelectron spectroscopy,” Chapter 9 in *Practical Surface Analysis*, D. Briggs and M. P. Seah, Eds., vol. 1, John Wiley & Sons, Chichester (1983).
64. J. Crane et al., “The application of electric fields to aerosol assisted chemical vapor deposition reactions,” *J. Electrochem. Soc.* **158**(2), D67 (2011).
65. G. Beamson and D. Briggs, *The Scienta ESCA 300 Database*, Wiley, Chichester (1992).
66. G. W. Coulston, E. A. Thompson, and N. Herron, “Characterization of VPO catalysts by X-ray photoelectron spectroscopy,” *J. Catal.* **163**(1), 122–129 (1996).
67. K. Zilberberg et al., “Solution processed vanadium pentoxide as charge extraction layer for organic solar cells,” *Adv. Energy Mater.* **1**(3), 377–381 (2011).
68. T. H. Lai et al., “Properties of interlayer for organic photovoltaics,” *Mater. Today* **16**(11), 424–432 (2013).
69. J. R. Manders et al., “Solution-processed nickel oxide hole transport layers in high efficiency polymer photovoltaic cells,” *Adv. Funct. Mater.* **23**(23), 2993–3001 (2013).
70. S. P. Cho et al., “Brush painted $V_2O_5$ hole transport layer for efficient and air-stable polymer solar cells,” *Sol. Energy Mater. Sol. Cells* **132**, 196–203 (2015).
71. J. S. Kim et al., “Control of the electrode work function and active layer morphology via surface modification of indium tin oxide for high efficiency organic photovoltaics,” *Appl. Phys. Lett.* **91**(11), 112111 (2007).
72. J. E. Houston et al., “Molecular design of interfacial layers based on conjugated polythiophenes for polymer and hybrid solar cells,” *Polym. Int.* **66**(10), 1333–1348 (2017).
73. V. D. Mihailetchi et al., “Photocurrent generation in polymer-fullerene bulk heterojunctions,” *Phys. Rev. Lett.* **93**(21), 216601 (2004).
74. J. Subbiah et al., “A green route to conjugated polyelectrolyte interlayers for high-performance solar cells,” *Angew. Chem. Int. Ed.* **56**(29), 8431–8434 (2017).

Biographies of the authors are not available.